

## Supplemental information

### Ultrafast Charge-discharge Characteristics of Nanosized Core-Shell Structured LiFePO<sub>4</sub> material for Hybrid Supercapacitor Applications

*Katsuhiko Naoi*<sup>\*1,2,3,4</sup>, *Kazuaki Kisu*<sup>1,4</sup>, *Etsuro Iwama*<sup>1,4</sup>, *Shota Nakashima*<sup>1</sup>, *Yuki Sakai*<sup>1</sup>, *Yuki Orikasa*<sup>5</sup>, *Philippe Leone*<sup>6</sup>, *Nicolas Dupré*<sup>6</sup>, *Thierry Brousse*<sup>4,6,8</sup>, *Patrick Rozier*<sup>4,7,8</sup>, *Wako Naoi*<sup>3</sup>, and *Patrice Simon*<sup>4,7,8</sup>

<sup>1</sup> Department of Applied Chemistry, Tokyo University of Agriculture & Technology, 2-24-16 Naka-cho, Koganei, Tokyo 184-8588, Japan

\*E-mail: [k-naoi@cc.tuat.ac.jp](mailto:k-naoi@cc.tuat.ac.jp)

<sup>2</sup> Advanced Capacitor Research Center and Tokyo University of Agriculture & Technology, 2-24-16 Naka-cho, Koganei, Tokyo 184-8588, Japan

<sup>3</sup> Division of Art and Innovative Technologies, K & W Inc, 1-3-16-901 Higashi, Kunitachi, Tokyo 186-0002, Japan

<sup>4</sup> Global Innovation Research Organization, Tokyo University of Agriculture & Technology, 2-24-16 Naka-cho, Koganei, Tokyo 184-8588, Japan

<sup>5</sup> Graduate School of Human and Environment Studies, Kyoto University, Yoshida-nihonmatsu-cho, Sakyo-ku, Kyoto 606-8501, Japan

<sup>6</sup> Institut des Matériaux Jean Rouxel (IMN), UMR 6502, Université de Nantes, CNRS, rue Christian Pauc, BP50609, 44306 Nantes Cedex 3, France

<sup>7</sup> CIRIMAT, Université de Toulouse, CNRS, INPT, UPS, 118 route de Narbonne 31062 Toulouse cedex 9, France

<sup>8</sup> Réseau sur le Stockage Electrochimique de l'Energie (RS2E), FR CNRS 3459

### Structural characterizations of the LFP/Carbon composites

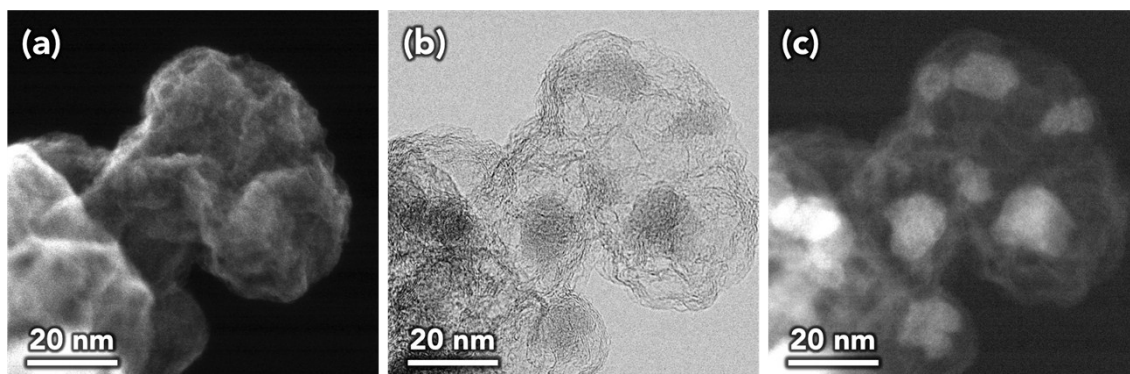


**Figure S1.** (a) Scanning electron microscope (SEM), (b) bright-field, and (c) dark-field images of the UC-derived LFP/graphitic carbon composites.

**Table S1.** Experimental Mössbauer parameters for M2 site ( $\text{Fe}^{2+}$ ), d-M2 site ( $\text{Fe}^{2+}$ ) and d-M2 site ( $\text{Fe}^{3+}$ ) in LFP/graphitic carbon composite.

	M2 site ( $\text{Fe}^{2+}$ )	d-M2 site ( $\text{Fe}^{2+}$ )	d-M2 site ( $\text{Fe}^{3+}$ )
Isomer shift / $\text{mm s}^{-1}$	1.18	1.20	0.40
Quadrupole split / $\text{mm s}^{-1}$	2.84	2.21	0.85

### **XPS measurements with Ar-etching (0 - 500s)**

The XPS data obtained after increasing duration of Ar-etching shows that above 20 s a slight intensity at 708 eV appears. This is the evidence of the presence of Fe<sup>0</sup> indicating that Ar-ion etching has brought about unwanted reduction of Fe species to the metal state thus destroying LFP compound. Therefore, we used the data within 14 s that would be reasonable to judge the valence of Fe as a function of depth of the composite.

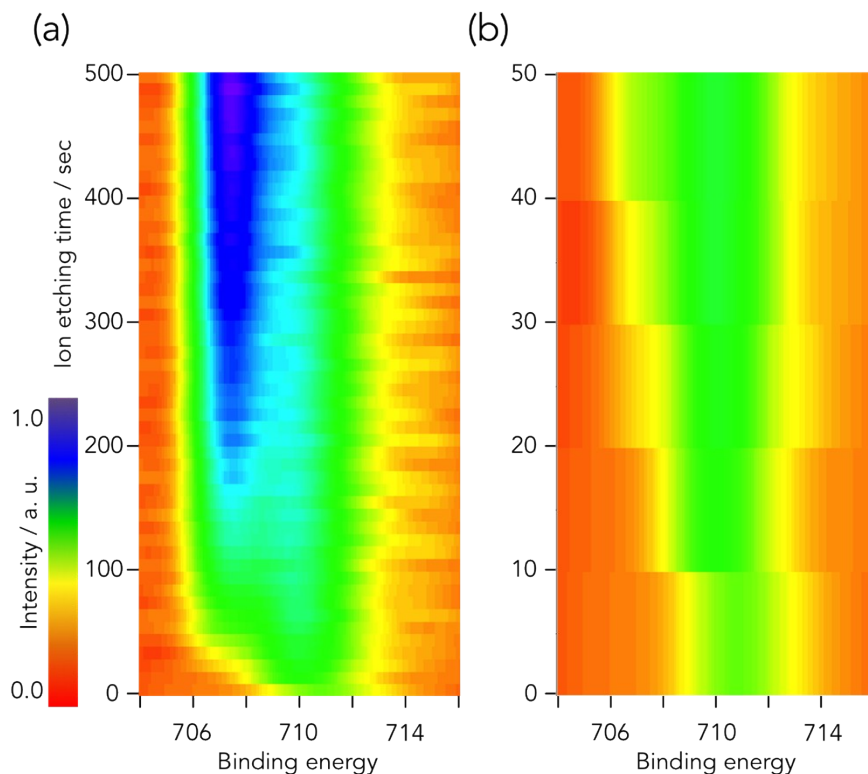


**Figure S2.** Consecutive XPS (Fe 2p core peaks) measurements with Ar-ion etching in (a) deep (0-500 s) and (b) shallow (0-50 s) durations. Data were acquired at 10 s intervals for both (a) and (b).

### **The role of TEM observations on uc-LFP/graphitic carbon composites**

TEM observations were made only as supporting experiments, to try to visualize the phases and get a better view of the structure of the composite. TEM experiments were carried out on more than three samples and all confirmed the presence of the amorphous phase. The representative images of (a), (b), and (c) focusing on the core-shell structure are shown in Figure S3.

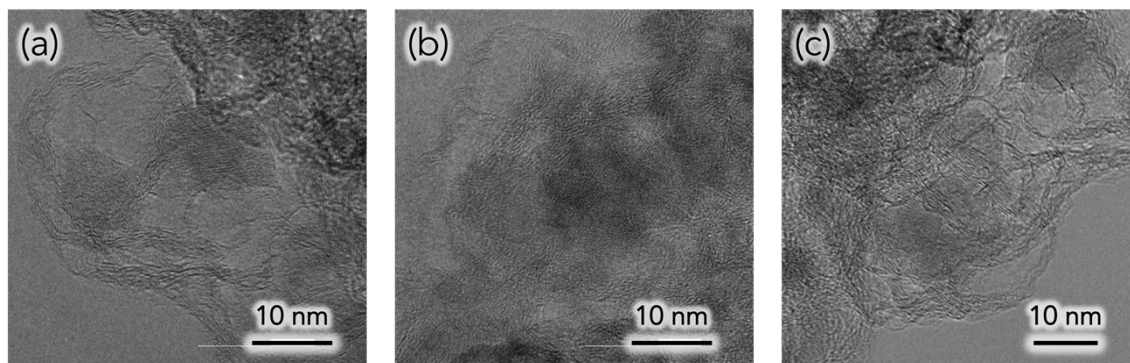


**Figure S3.** HRTEM images of LFP/graphitic carbon composite at different spots.

The ratio of amorphous vs. crystalline LFP phase was determined based on the electrochemical signature of the composite, from the plateau and the sloping discharge capacities corrected from the carbon double layer. This method is certainly an accurate method since i) the electrochemical signatures of the two phases are different and can be easily identified and ii) this is confirmed by the *in situ* XRD patterns which show that part of the electrochemical process involves changes in the XRD pattern (crystalline phase) while others do not affect the XRD pattern (amorphous phase). As discussed later in Figure S10, we found that the crystalline vs. amorphous weight ratio was 31/69 by weight and 25/75 by volume based on the estimated densities of the materials.

### **Thermogravimetric analysis**

Thermogravimetric analysis (TGA) was used to investigate the interaction between LFP core and the graphitic carbon shell. Many previous publications reported a decrease of the combustion temperature for carbon material vs. pristine carbon when carbon is combined with inorganic nanoparticles such as metal oxides or phosphate.<sup>[1]</sup> Figure S4 shows the TGA of uc-treated KB (uc-KB) sample. Compared to the oxidation of uc-KB particles observed at 654°C, the decomposition of the LFP/graphitic carbon composite is observed at lower temperatures (468°C). Such a decrease could be partially explained by the catalytic effect of the inorganic nanoparticles on the oxidative decomposition of carbon.<sup>[2]</sup> However, the decrease of the decomposition temperature also depends on how the LFP particles are connected with the graphitic carbon; on surface, inner tubes, edges, or crystallized on amorphous.

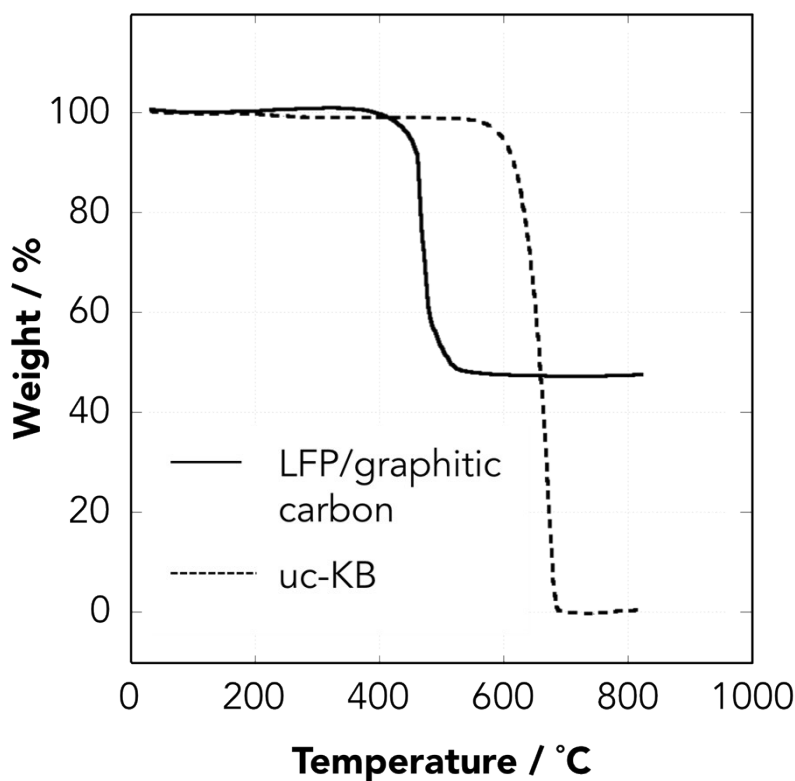


**Figure S4.** TGA curves for LFP/graphitic carbon composite and a uc-treated KB (uc-KB) sample used as reference. TGA measurements were performed at a sweep rate of 10°C min<sup>-1</sup> from ambient temperature to 800°C under a synthetic air atmosphere.

**Elemental mapping for Li, Fe, P and O in the composite**

Elemental mapping was achieved using electron energy loss spectroscopy to observe the distribution of Li, Fe, P and O in the composite (EELS; Figure S5). STEM image shows that while iron, phosphorus, and oxygen are localized in the light contrast particle, Li ions are distributed over a large area, including the locations where P, Fe, O are present in the LFP particle. Interestingly, Li-distribution area overlaps the carbon-distribution area (Figure S6). This suggests that the graphitic carbon shell contain intercalated Li-ions thus improving the electrical conductivity of the composite.

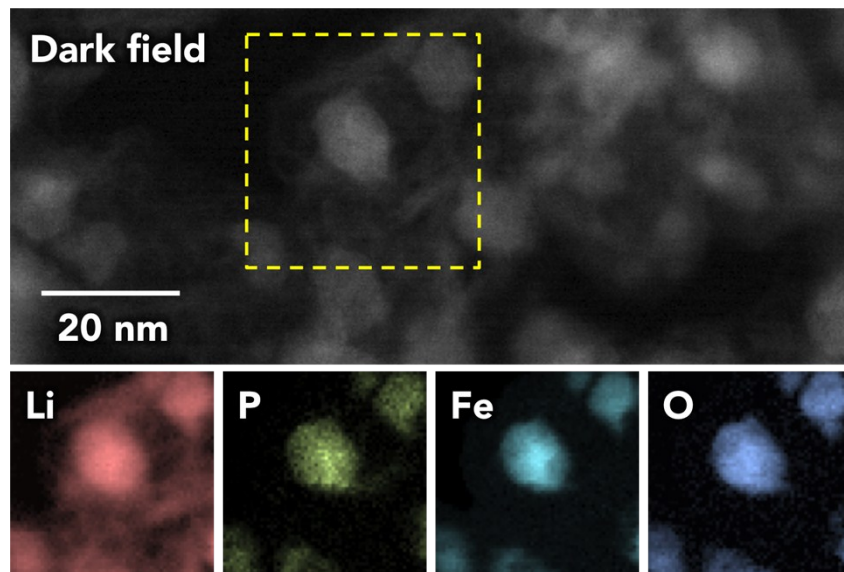


**Figure S5.** Dark field image of the pristine LFP/graphitic carbon composite and the EELS maps of lithium, phosphorous, iron, and oxygen measured in the part enclosed with yellow dash square.

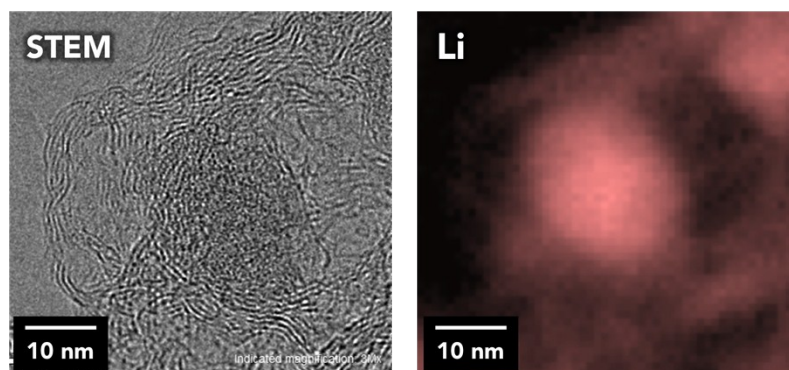


**Figure S6.** STEM image and EELS maps of lithium in the same location of the LFP/graphitic carbon composite.

### **The role of carbon shell**

Aside the LFP/graphitic carbon composite, uc-LFP without KB was prepared using UC-treatment. However, the material resulted in large, agglomerated, LFP crystalline that turned to show poor electrochemical performance when tested under the same conditions. And also, thermal treated composite was prepared to remove the graphitic carbon shell under air atmosphere at 700°C. This experiment resulted in substantial agglomeration (see Figure S7) and increased particle size, leading to degraded rate-capability performance. So, this experiment certainly gives an insight to the role of carbon shell, which is clearly very important to maintain the peculiar “nano-sized” morphology.

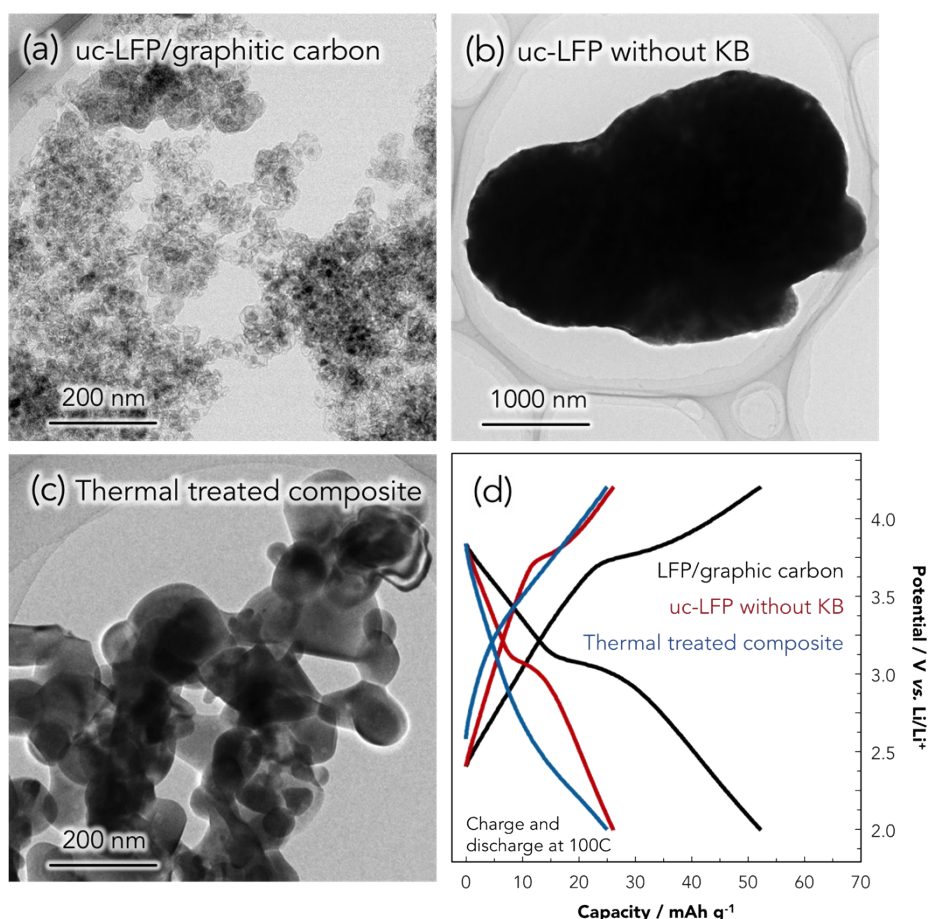
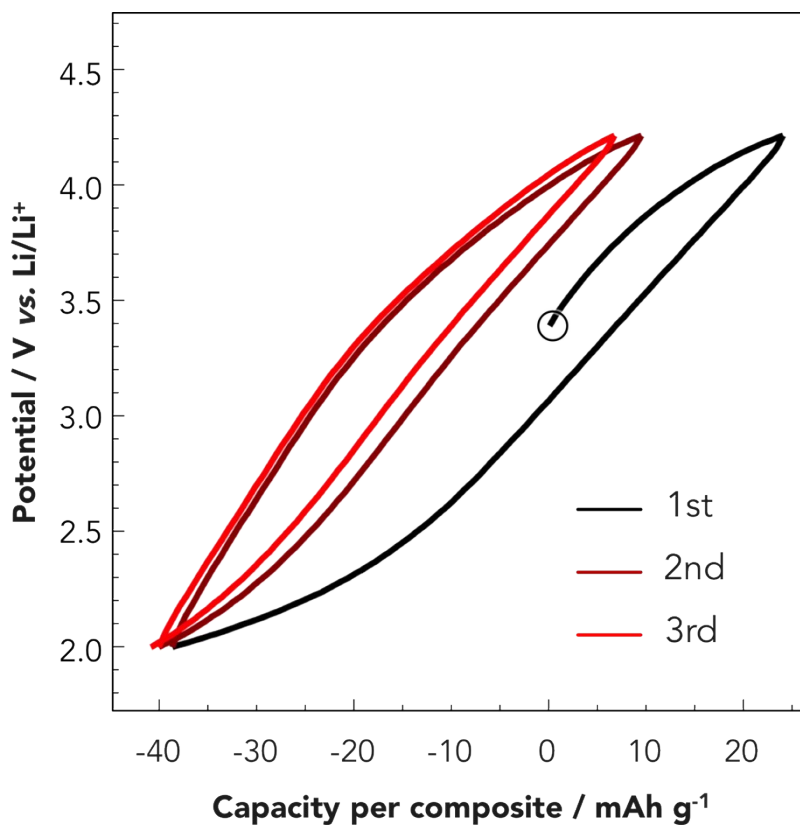


Figure S7. HRTEM images of the composite formation for (a) uc-LFP/graphitic carbon composite, (b)uc-LFP without KB, and (c) thermal treated composite. (d) Charge-discharge curves of a half-cell consisting of each sample at a 100C rate.

### Electrochemical signatures of uc-KB for initial three cycles

To investigate the electrochemical behavior of the uc-KB, charge-discharge tests were performed in a half-cell Li/uc-KB at 1C rate ( $1C = 50 \text{ mA g}^{-1}$ ), within 2.0–4.2 V vs. Li/Li<sup>+</sup> voltage range for the first three cycles (Figure S8). At the 1<sup>st</sup> charge, a low capacity of  $24 \text{ mA h g}^{-1}$  per uc-KB is obtained. On the other hand, after the 1<sup>st</sup> discharge process, a reversible capacity of  $49 \text{ mA h g}^{-1}$  per uc-KB is obtained.



**Figure S8.** Charge-discharge curves (1<sup>st</sup>- 3<sup>rd</sup> cycle) of a half cell consisting of Li/1M LiPF<sub>6</sub> EC+DEC/uc-KB composite at a 1C rate.

### Cycle performance at 60C and 240C

Additionally, we have cycled more than 2000 times at 60C and 240C as shown in Figure S9. There appear initial increases in the capacity up to 200-250 cycles depending upon the rate. The capacity after 2000 cycles was found to be 92% and 96% of the maximum capacity, for 60C and 240C discharge respectively.

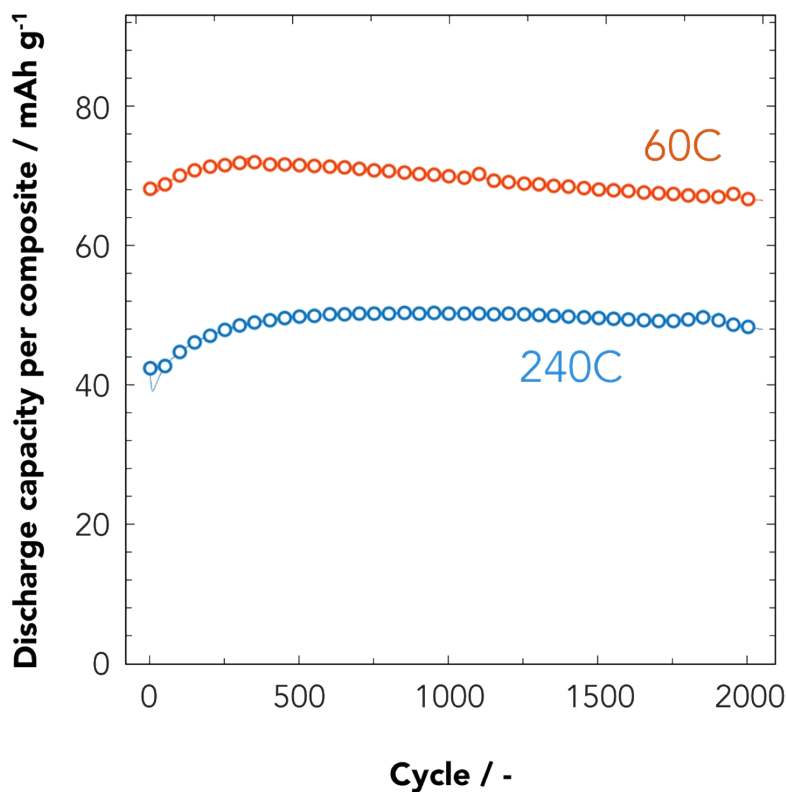


**Figure S9.** Change of the discharge capacity for the uc-LFP/graphitic carbon composite electrodes at two C-rates, versus the cycle number.

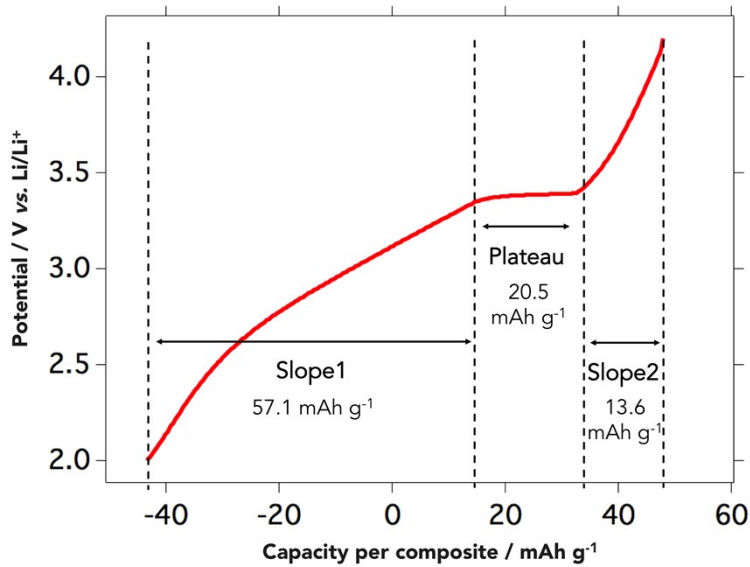
### **Calculation of Fe valence state using XAFS measurement**

The redox states of Fe were investigated by *in situ* X-ray absorption fine structure (XAFS) measurements at the SPring-8 synchrotron during the initial three charge-discharge tests. The Fe K-edge spectra include information on transitions from the 1s to the 3d unoccupied orbitals. During the delithiation and lithiation of Fe compounds, the electron transfer occurs to and from the 3d orbital, respectively, and the absorption edge shifts toward higher energy. The threshold energy position (Fe) of the absorption edge gives information about the valence state of the probing atom. The average valence state of Fe is determined by the deconvolution of the spectra using the contributions of Fe<sup>2+</sup> and Fe<sup>3+</sup> based on commercial LFP (Fe<sup>2+</sup>) and oxidized LFP (Fe<sup>3+</sup>) used as standards.

### **Ratio of the crystalline/amorphous phases**

To address the weight ratio for the crystalline/amorphous phases, an approach of electrochemical signature was taken. From a representative discharge curve as indicated in Figure S10, we try to separately estimate the capacities from the plateau region (crystalline LFP) and from the sloping region (amorphous LFP + KB contribution). The capacity ratio (by weight) for the crystalline/amorphous regions was found to be 20.5/45.5 that is a composition of 31% of crystalline LFP and 69% of amorphous LFP.

$$\begin{aligned} \text{Ratio} &= C(\text{crystalline}) / C(\text{amorphous}) \\ &= 20.5/45.5=0.45= \underline{31/69} \end{aligned}$$



C (crystalline) (Plateau)	: 20.5 mAh g <sup>-1</sup>	31%
C (amorphous + KB) (Slope1 + 2)	: 70.7 mAh g <sup>-1</sup>	
C (Amorphous)	: 45.5 mAh g <sup>-1</sup>	69%
C (KB)	: 25.2 mAh g <sup>-1</sup>	

**Figure S10.** Discharge curve (3<sup>rd</sup> cycle) of a half-cell consisting of Li/1M LiPF<sub>6</sub> EC+DEC(vol. 1:1)/(LFP/graphitic carbon) composite at a 1C rate, with the estimation of each capacity for the crystalline LFP and amorphous LFP.

### Calculation of diffusion coefficient of LFP/graphitic carbon using GITT method

Lithium-ion diffusion coefficient was calculated using the galvanostatic intermittent titration technique (GITT) using Equation (1),

$$D_{\text{Li}^+} = 4/\pi\tau ((m_B V_M)/(M_B A))^2 (\Delta E_s/\Delta E_\tau)^2, \text{ Eq(1)}$$

where  $V_M$ ,  $M_B$ ,  $m_B$ , are the molar volume ( $\text{cm}^3$ ), molecular weight of the LFP ( $\text{g mol}^{-1}$ ), weight of LFP (g) respectively,  $A$  is the total contact area between the electrolyte and the electrode ( $\text{cm}^2$ ).  $\Delta E_s$  (V) and  $\Delta E_\tau$  (V) are the total transient change in potential after subtracting the IR drop and the change in the steady-state voltage during the respective single titration current. [3, 4] Figure S11 shows the discharge curve and Li-ion diffusion coefficient ( $D_{\text{Li}^+}$ ).

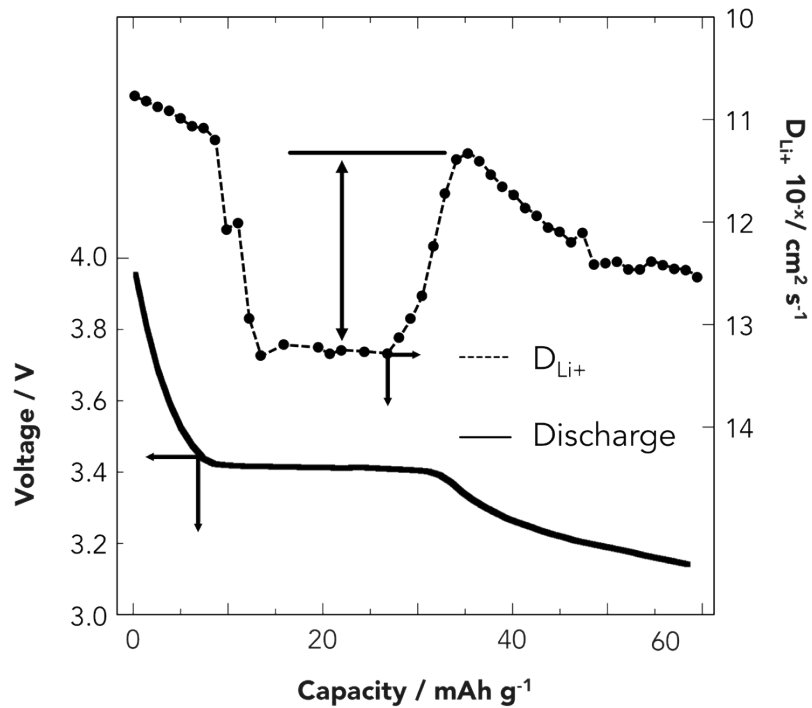


**Figure S11.** Galvanostatic intermittent titration technique (GITT) analysis in the voltage range of 3.1–4.0 V, with the  $\text{Li}^+$  diffusion coefficients calculated from the GITT curves.

**The effect of carbon content to the encapsulated LFP cores**

The size of the encapsulated LFP cores did not change essentially by varying annealing time (5 min-2 hrs) or annealing temperature (700-800°C) at a fixed ratio of carbon content (50w%)(see Figure S12(a)). However, decreasing the carbon content below 30w% (see Figure S12(b)) drastically increased the LFP particle size, which is not anymore encapsulated.

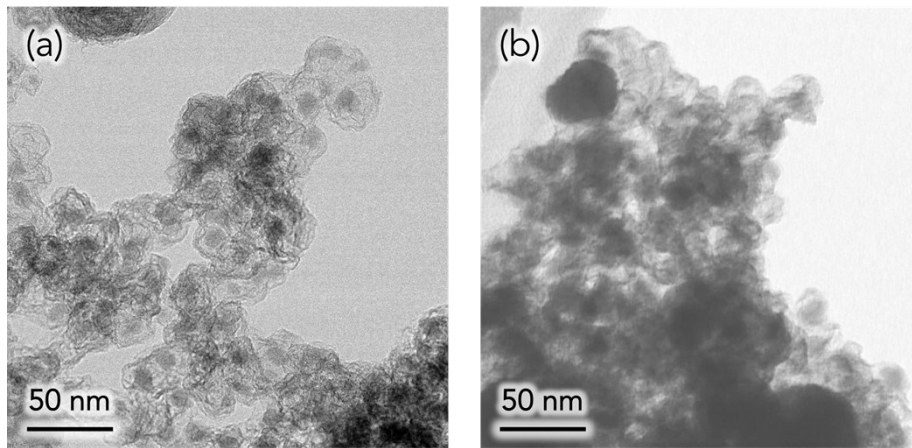


**Figure S12.** HRTEM images of LFP/graphitic carbon composites; (a) 50w% and (b) 30w%.

**Feasibility test as a hybrid full cell**

We have tested a full cell configured as AC (20 $\mu$ m)/1M LiPF<sub>6</sub> (EC+DEC)/uc-LFP(20 $\mu$ m) as shown in Figure S13. The capacity ratio of anode/cathode was set as 1/1, so the weight ratio of the AC /uc-LFP being 2/1. The voltage range tested was 0-2.7V at a current density of 34 mA g<sup>-1</sup> (per LFP). Typical charge-discharge curves at third cycle are shown. The hybrid full cell delivers 41 F g<sup>-1</sup>, which is 1.3 times higher than a reference cell (AC/AC in the same electrolyte). This is a small demonstration of a hybrid cell concept and it shows feasible for further testing. Note as well that the electrochemical response of the crystalline LFP phase is observed, contributing to the improvement of the cell capacitance and energy.

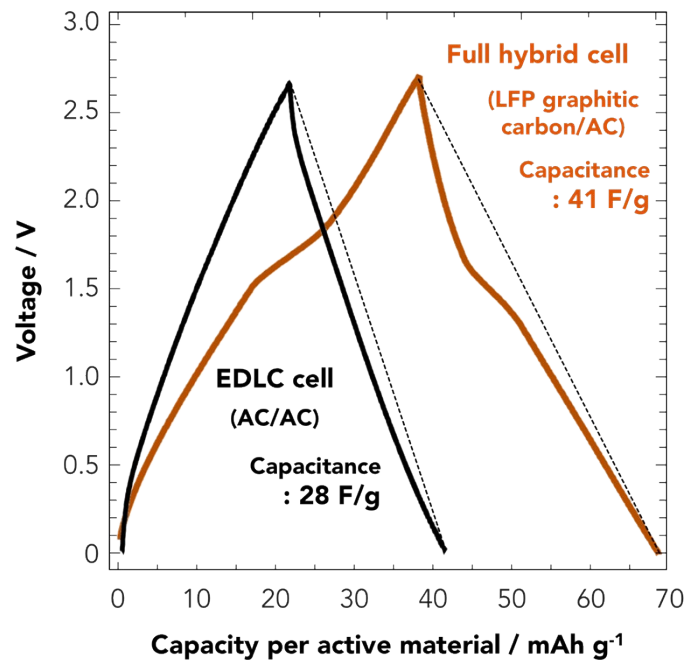


**Figure S13.** Comparison of the voltage profiles of a symmetric AC/AC and a hybrid AC/uc-LFP cells.

**The encapsulation mechanism during drying and annealing processes.**

We are currently working on the understanding of the reaction mechanism during the uc treatment process. However, based on all the experiments we have done, we start to have a better understanding of the processes. After UC treatment, the sample is subjected to the drying process at 80°C *in vacuo*. During this step, we assume that the water media containing Fe, Li, PO<sub>4</sub> sources, and other chelating agents get concentrated within the hollows of graphitic carbon shell due to capillary effect, leading to the formation of LFP particles in the inner KB instead of outside.

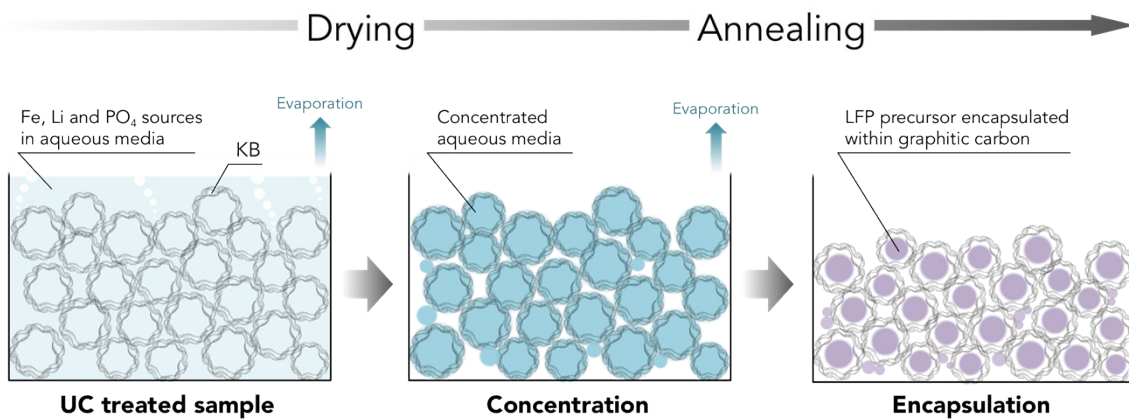


**Figure S14.** Illustrations of the encapsulation mechanism during drying and annealing processes.

Then during annealing at 700°C, the media evaporates faster in outer shells than inner composite shells. Thereby, the media as well as the LFP-precursor may become more and more concentrated and confined in inner shells. During annealing process, the confined LFP-precursor gets crystallized to become the LFP core part. We also speculate that in the vicinity of outer shells the LFP-precursor has more interference with the graphitic carbons preventing full crystallization resulting in partial crystallized or amorphous phases. Therefore the resulting LFP nanoparticles are configured generally as core crystalline and amorphous outer sphere.

## References

- [1] B. Gao, C. Peng, G. Z. Chen and G. L. Puma, *Applied Catalysis B-Environmental*, 2008, **85**, 17-23.
- [2] E. Kockrick, L. Borchardt, C. Schrage, C. Gaudillere, C. Ziegler, T. Freudenberg, D. Farrusseng, A. Eychmüller and S. Kaskel, *Chem. Mater.*, 2011, **23**, 57-66.
- [3] K. M. Shaju, G. V. Subba Rao and B. V. R. Chowdari, *J. Electrochem. Soc.*, 2003, **150**, A1-A13.
- [4] K. M. Shaju, G. V. Subba Rao and B. V. R. Chowdari, *J. Mater. Chem.*, 2003, **13**, 106-113.